Resonant photoemission spectroscopy of the ferromagnetic Kondo system CeAgSb 2

Chien-Wen Chuang, Bodry Tegomo Chiogo, Daniel Malterre, Pei-Yun Chuang, Cheng-Maw Cheng, Tun-Wen Pi, Fan-Hsiu Chang, Hong-Ji Lin, Chien-Te Chen, Chia-Nung Kuo, et al.

Electronic Structure

PAPER

Resonant photoemission spectroscopy of the ferromagnetic Kondo system $CeAgSb_2$

C W Chuang[1], B Tegomo Chiogo[2], D Malterre[2], P-Y Chuang[1], C-M Cheng[1], T-W Pi[1], F-H Chang[1], H-J Lin[1], C-T Chen[1], C-N Kuo[3], C-S Lue[3] and A Chainani[1,*]

[1] National Synchrotron Radiation Research Center, Hsinchu 30076, Taiwan, Republic of China
[2] Université de Lorraine, CNRS, Institut Jean Lamour, F-54000 Nancy, France
[3] Department of Physics, National Cheng Kung University, Tainan 70101, Taiwan, Republic of China
[*] Author to whom any correspondence should be addressed.

E-mail: chainani.ash@nsrrc.org.tw

Keywords: Kondo material, resonant photoemission spectroscopy, x-ray absorption spectroscopy

Abstract

We study the electronic structure of single crystal $CeAgSb_2$, a low T_c ferromagnetic Kondo system, using synchrotron radiation photoemission spectroscopy (PES) and x-ray absorption spectroscopy (XAS). We have carried out Ce 5*s*, Ce 5*p*, Sb 4*d* core level PES as well as Ce 4*d*–4*f* resonant PES of the valence band states of $CeAgSb_2$. We also report the resonant PES behavior of Ce 5*s* and 5*p* core-levels and the simultaneous intensity suppression of Sb 4*d* core-level and Ag 4*d* valence band states across the Ce 4*d*–4*f* threshold. The Ce 4*d*–4*f* resonant valence band spectra show typical f^0 and f^1 features associated with Kondo behavior. The constant initial state spectra of the f^0 and f^1 features show maxima at different incident photon energies, arising from different relative contributions of surface and bulk character Ce 4*f* partial density of states. XAS across the Ce 3*d*–4*f* *M*-edge also shows the corresponding final state f^1 and f^2 features. The weak temperature dependence of the XAS spectra between $T = 25$ K and 300 K could be simulated using a full multiplet calculation combined with a simplified single-impurity Anderson model approach. The calculations confirm the Kondo screening and allows quantification of the bulk Ce 4*f* electron count in $CeAgSb_2$. The Ce 5*s* states show an exchange splitting which reflects the local magnetic moment of Ce 4*f* states. The overall results characterize the bulk and surface sensitive Ce 4*f* states, and indicate the role of Kondo effect in forming the moderately enhanced heavy-fermion carriers in $CeAgSb_2$.

1. Introduction

Strongly correlated Ce and Yb based 4*f* electron systems often exhibit a competition between the Kondo effect and Ruderman–Kittel–Kasuya–Yosida (RKKY) interaction [1–5]. When the Kondo effect is stronger than the RKKY interaction, it results in a non-magnetic Kondo singlet ground state. On the other hand, when the RKKY interaction is stronger, it results in a ferro- or antiferro-magnetically ordered ground state [1–3]. The competition between the two can be usually identified from temperature dependent electrical transport and magnetic susceptibility studies which show clear signatures of the Kondo effect and magnetic order, respectively [2, 3]. Among such systems, the series $CeTX_2$ (where T = Au, Cu, Ni, Pd and Pt; X = *p*-block element) form an interesting class of materials, which exhibit magnetic or non-magnetic ground states as well as Fermi or non-Fermi liquid behavior at low temperatures. For example, $CeCuAs_2$ exhibits a non-Fermi liquid behavior without magnetic order down to the lowest measured temperature of 45 mK [6]. On the other hand, $CePtGe_2$ exhibits an antiferromagnetic ordering below 3.8 K and Fermi-liquid like behavior at lower temperatures [7]. The $CeTX_2$ compounds exhibit the primitive tetragonal $ZrCuSi_2$ type structure ($P4/nmm$, No. 129) consisting of X–CeX–T–CeX–X layers stacked along the *c*-axis [8]. The character of Ce 4*f* electrons, the electron configuration of transition metal ion T, and how the Ce 4*f* electrons hybridize with the nearest neighbor *p*-block anions X in the Ce–X layers mainly determines the properties of these systems [9].

In this study, we investigate the electronic structure of the Kondo material $CeAgSb_2$, which crystallizes in the $ZrCuSi_2$ structure and exhibits lattice parameters $a = b = 4.363$ Å, and $c = 10.699$ Å [8]. Magnetization measurements of $CeAgSb_2$ revealed an unusual magnetic transition at $T_c \sim 9.8$ K [10–13]. The detailed analysis of magnetization of $CeAgSb_2$ showed a magnetic anisotropy below T_c with dominantly ferromagnetic behavior for $H \parallel c$ axis and weakly antiferromagnetic behavior for $H \perp c$ axis (hereafter, we refer to this transition as a ferromagnetic transition). The high temperature inverse susceptibility data suggested a Kondo temperature T_K of ∼65 K, which is comparable to the value estimated from inelastic neutron scattering [10] as well as muon spin rotation measurements [14]. The field dependence of magnetization showed a magnetic saturation of 0.4 μ_B/Ce along the c axis due to the ground state wave function with $J_z = |\pm\frac{1}{2}\rangle$, which is in agreement with the calculated saturation moment $g_j\mu_B J_z = 0.43\ \mu_B$/Ce. Further, the total magnetic susceptibility could be fitted using the first and second excited states at ∼60 K and ∼145 K, which correspond to the $J_z = \frac{3}{2}$ and $\frac{5}{2}$ states, respectively [13]. This result matches nicely with the results of the crystalline electric field levels determined by neutron scattering measurements [10].

The temperature dependence of the electrical resistivity of $CeAgSb_2$ showed a logarithmic increase for temperatures below 150 K, indicating a Kondo lattice system [13]. On further lowering the temperature the resistivity showed a maximum at ∼15 K followed by a dramatic decrease below $T_c = 9.8$ K, which corresponds to the ferromagnetic transition temperature. At the lowest temperatures, it was shown that $CeAgSb_2$ exhibited a Fermi-liquid type behavior, but with an additional contribution due to the electron-magnon scattering [13]. Heat capacity measurements showed that $CeAgSb_2$ exhibits a Sommerfeld coefficient $\gamma = 65$ mJ mol^{-1} K^2, which corresponds to a mass enhancement of ≈21 compared to iso-structural $LaAgSb_2$, indicative of a moderately enhanced heavy-fermion behavior [15].

High energy spectroscopies such as PES and XAS have played an important role in characterizing the electronic structure of Kondo materials [4, 5]. The electronic structures of many Ce and Yb compounds could be explained based on the single impurity Anderson model (SIAM) calculations developed by Gunnarsson and Schonhammer [16, 17]. The model takes into account f^0, f^1 and f^2 basis states hybridizing with a conduction band. The hybridization between the strongly correlated atomic f orbital basis states gives rise to a Kondo resonance just about the Fermi level E_F. This Kondo resonance leads to a renormalization of carriers, which is responsible for the electronic transport and the non-magnetic Kondo singlet formation [4, 5].

An early ultra-violet angle resolved photoemission spectroscopy (ARPES) showed highly dispersive Sb bands near E_F [18]. This study also identified a hole-like Fermi surface at the Brillouin zone center in agreement with a band calculation of $LaAgSb_2$, which is the non-f isostructural analogue of $CeAgSb_2$. In a soft x-ray spectroscopy study, Saitoh *et al* [19] reported on magnetic circular dichroism and ARPES results, and concluded that $CeAgSb_2$ exhibits local magnetism and hybridization effects between Ce 4f level and conduction electrons. From Ce 3d–4f on resonance measurements, the study also showed that Ce 4f states occurred at the Fermi level. In a very recent study, using linearly polarized hard x-ray photoemission spectroscopy (HAXPES) study of Ce 3d core levels, Fujiwara *et al* could successfully show that ground state symmetry of Ce 4f states in $CeAgSb_2$ exhibits Γ_6 symmetry with $J_z = |\pm\frac{1}{2}\rangle$, consistent with the magnetic susceptibility and neutron scattering results [20]. However, a quantification of the small expected mixed valency of f-electron states has not been carried out to date.

In this work, we report low energy ($h\nu = 108$–132 eV) synchrotron radiation PES and Ce 3d–4f XAS of $CeAgSb_2$. We measured the photon energy dependent valence band as well as the Ce 5s, Ce 5p, Ag 4p, and Sb 4d core levels of $CeAgSb_2$ across the Ce 4d–4f threshold. Constant initial state (CIS) spectra identify a clear Fano-resonance behavior in the f^0 and f^1 features in the valence band spectra. The results also show systematic changes in the spectral weight of the Ag 4d valence band states as well as the core level spectra. The near E_F spectral intensity shows the Ce $4f^1_{7/2}$ feature at ∼0.3 eV and the $4f^1_{5/2}$ feature at E_F associated with the tail of the Kondo resonance above E_F. A full multiplet calculation combined with a simplified SIAM approach confirms the role of Kondo screening in explaining all the spectral features of the Ce 3d–4f XAS spectra and provides a quantification of the bulk Ce 4f electron count and small finite mixed valency in $CeAgSb_2$. The results indicate the role of Kondo screening in forming the moderately enhanced heavy fermion carriers in $CeAgSb_2$.

2. Experimental methods

Single crystals of $CeAgSb_2$ were synthesized using stoichiometric amounts of the constituent elements (>99.9% purity), as described in earlier work [10–13]. The crystal structure and lattice constants were confirmed to be in good agreement with reported results [8, 10]. Core-level and valence band PES ($h\nu = 108$ to 132 eV) measurements were carried out at beamline BL8A of the Taiwan Light Source, Hsinchu, Taiwan. The total energy resolution for photoemission spectroscopy was 0.4 eV at $h\nu = 132$ eV as estimated from a fit to the Fermi-edge of gold at $T = 80$ K, which was also used to calibrate the binding energy (BE) scale. The samples were cleaved inside the UHV preparation chamber at a pressure of 5×10^{-8} mbar and immediately transferred

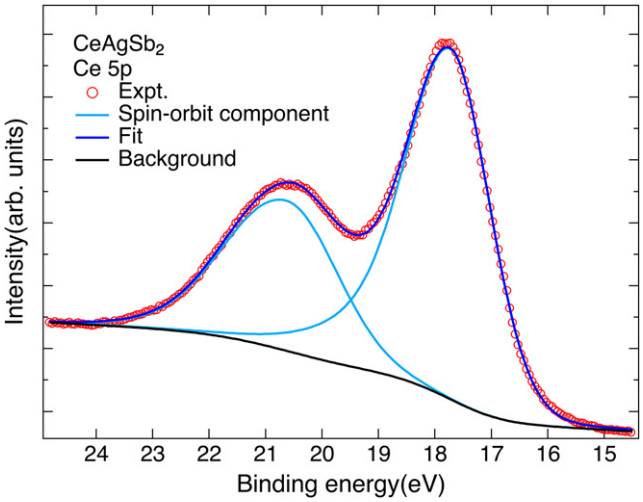

Figure 1. The Ce 5*p* core-level photoemission spectrum of $CeAgSb_2$ measured at $T = 80$ K using photon energy $h\nu = 115$ eV. The least squares fitting results is also shown together with experimental spectrum. The fitting results are listed in table 1.

Table 1. The least squares fit parameters for the Ce 5*p* core-level spectrum.

Spin–orbit component	BE (eV)	FWHM (eV)	Asymmetry parameter
Ce $5p_{3/2}$	17.73	1.83	0.28
Ce $5p_{1/2}$	20.64	2.36	0.35

to the main chamber at 8×10^{-10} mbar for PES measurements. XAS experiments across the Ce 3*d*–4*f M*-edge were performed using circularly polarized x-rays at the Dragon beamline BL11 of Taiwan Light Source and the samples were cleaved *in situ* in the main chamber. The sample was cooled using a liquid N_2 flow-type cryostat down to 80 K for photoemission measurements, while a liquid He flow-type cryostat was used to go down to 25 K for the XAS experiments. All measurements were carried out within 8 h of cleaving and confirmed to be reproducible from two different cleaves for both, PES and XAS experiments. The oxygen 2*s* shallow core level energy range was measured and it showed negligible intensity (<1%) compared to the Ce 5*p* PES spectra. Similarly, the oxygen *K*-edge XAS signal was measured to be negligible (<1%) compared to the Ce *M*-edge XAS spectra.

3. Results and discussions

Figure 1 shows the Ce 5*p* core-level photoemission spectrum of $CeAgSb_2$ measured using a photon energy $h\nu = 115$ eV at a temperature of $T = 80$ K. The Ce 5*p* spectrum shows two clear peaks which are the $5p_{3/2}$ and $5p_{1/2}$ spin–orbit split features. The BE of the spin–orbit split features were accurately determined by a least-squares fitting with a Shirley background and asymmetric Doniach–Sunjic type Voigt profiles. The fitting results of Ce $5p_{3/2}$ and $5p_{1/2}$ are also plotted along with the experimental spectrum. The least-squares fit parameters are shown in table 1. From the results, we obtain the BE positions of Ce $5p_{3/2}$ and the Ce $5p_{1/2}$ to be 17.73 eV and 20.64 eV, respectively. The energy separation between Ce $5p_{3/2}$ and $5p_{1/2}$ is 2.91 eV and the measured intensity ratio of Ce $5p_{3/2}$ and $5p_{1/2}$ states is 2.01. This is very close to the expected value of 2 as it is simply proportional to their multiplicities.

Next, we used the same photon energy of $h\nu = 115$ eV to measure the Sb 4*d* and Ce 5*s* core-level spectra of $CeAgSb_2$ at $T = 80$ K, as shown in figure 2. The Sb $4d_{5/2}$ and $4d_{3/2}$ spin–orbit split features occur between BEs of 30 to 34 eV, and a weak broad feature originating in the Ce 5*s* states are observed at a higher BE of about 36 eV. In order to understand the spectral shapes and obtain accurate BE positions of the Sb 4*d* and Ce 5*s* features, we used the same fitting method as for the Ce 5*p* spectrum to fit the Sb 4*d* and Ce 5*s* core-level spectra of $CeAgSb_2$. The fitting results are also shown in figure 2 along with the experimental data. The parameters of the fitting are listed in table 2. From the fitting results, the Sb $4d_{5/2}$ and $4d_{3/2}$ are positioned at BEs of 31.37 and 32.62 eV, respectively. The spin–orbit splitting of Sb 4*d* states is 1.25 eV and their measured intensity ratio is 1.49, consistent with the expected ratio of their multiplicities of 6:4. It is known that some

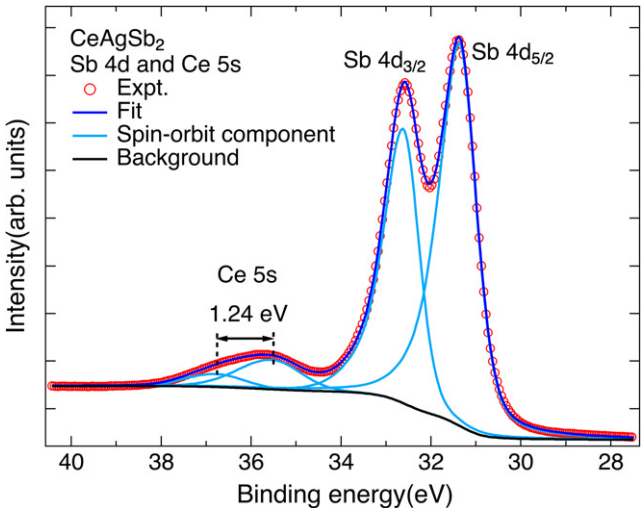

Figure 2. The Sb 4*d* and Ce 5*p* core-level spectrum of $CeAgSb_2$ measured at $T = 80$ K using photon energy $h\nu = 115$ eV. The least-squares fit is also shown along with experimental spectrum. The fitting parameters are listed in table 2.

Table 2. The least squares fit parameters for the Sb 4*d* and Ce 5*s* core-level spectra.

Spin–orbit component	BE (eV)	FWHM (eV)	Asymmetry parameter
Sb $4d_{5/2}$	31.37	1.00	0.30
Sb $4d_{3/2}$	32.62	0.95	0.30
Ce $5s^3F$	35.55	1.66	0.30
Ce $5s^1F$	36.79	1.51	0.20

Ce based materials like γ-Ce and CeAl exhibit a surface core-level shift (SCLS) in Ce 5*p* spectra with a surface component at 0.6 and 0.5 eV higher BE compared to the bulk component [21], while in CeSe, the Se 3*d* core levels exhibit SCLS with a surface component at 0.4 eV higher BE compared to the bulk component [22]. In the case of $CeAgSb_2$, the fitting of the Ce 5*p* and Sb 4*d* spectra using single peaks for the spin–orbit split doublet features, with the known spin–orbit splitting and with the expected intensity ratio indicates that the shallow core level spectra do not exhibit SCLS.

Interestingly, the Ce 5*s* spectrum also consists of a doublet as seen from the fitting results shown in figure 2. The absence of SCLS in the Ce 5*p* and Sb 4*d* spectra suggests that the splitting in Ce 5*s* is unlikely to be due to SCLS. It is well-known that the *s*-character core-level can show a splitting due to the exchange interaction between the core and valence electrons for a material with local magnetic moments at the same site. Since $CeAgSb_2$ shows a ground state ferromagnetic order below $T_c = 9.8$ K, we attribute the Ce 5*s* splitting to the exchange interaction between for Ce 5*s* and the local magnetic moment of Ce 4*f* states. The energy separation between the doublets is $\Delta E_{5s} = 1.24$ eV, and is a measure of the Ce 5*s*–4*f* exchange interaction. For the atomic Ce^{3+} case, the Ce 5*s* up- and down-spin $s = 1/2$ coupling with the spin $S = 1/2$ in the Ce 4*f* shell will result in the total spin $S' = S \pm s$ states, which are the ^3F and ^1F doublet states. The ^3F is positioned at lower BE and the intensity ratio is expected to be proportional to the multiplicities of ^3F and ^1F states i.e. 3:1. From the fitting results, we obtain a slightly smaller value for the intensity ratio of 2.72. It is known that the multiplet averaged exchange splitting $\Delta E_s = (2S_v + 1)J^{\text{eff}}_{s-f}$, where S_v is the valence magnetic moment of the photo-emitting site and J^{eff}_{s-f} is the *s*–*f* exchange integral. Thus, although the effective magnetic moment of Ce shows anisotropic behavior as discussed in the introduction, the small value of the experimental $\Delta E_{5s} = 1.24$ eV is consistent with earlier experimental results on Ce systems [23, 24].

With the aim of identifying the character of the electronic states in the valence band, we have measured the valence band photoemission spectra of $CeAgSb_2$ by varying the incident photon energy $h\nu$ from 108 to 132 eV across the Ce 4*d*–4*f* threshold at $T = 80$ K as shown in figures 3(a) and (b). As can be seen from the spectra, the spectral intensities of electronic states between E_F and 4 eV BE systematically increases on increasing the incident photon energy $h\nu = 108$ to 123 eV (figure 3(a)). On further increasing the incident photon energies above 123 eV, figure 3(b) shows that the spectral intensities of electronic states between E_F and 4 eV BE get systematically reduced.

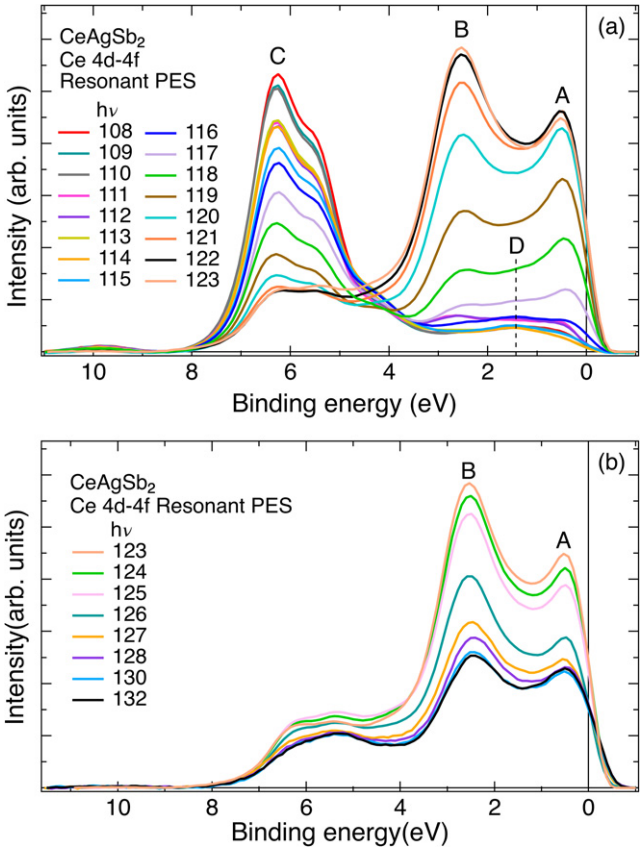

Figure 3. The valence band spectra of $CeAgSb_2$ measured at $T = 80$ K by systematically changing incident photon energies: (a) from 108 to 123 eV, and (b) from 123 to 132 eV.

In order to understand these spectral intensity changes, we have plotted the CIS spectra in figure 4, for features labeled A, B and C in figures 3(a) and (b). It is clear from the CIS spectra that the states between E_F to 4 eV BE exhibit a resonant behavior, which follows the Fano line shape overlaid on the CIS spectra for features A and B (figure 4). As is well known, the Ce 4*d*–4*f* resonance occurs at a photon energy of about 120–122 eV as reported in various Ce compounds [22, 25–31]. In the present case, feature A has a maximum at 121 eV, confirming that feature A originates from Ce 4*f* states. On the other hand, the feature B has a maximum intensity at 123 eV. This feature also originates from Ce 4*f* states. The features A and B have been observed in several Ce systems earlier and they originate in the f^0 and f^1 features associated with direct photoemission channel of the Ce^{3+} and the tail of the Kondo resonance feature just above E_F. The difference in resonance energy maximum for feature A and B is due to the dominant contribution of the bulk and surface character f^0 and f^1 states, namely, feature A has dominant bulk character while feature B has dominantly surface character [29, 30]. It is noted that in figure 4, there is a small bump feature in the CIS spectra for features A and B between photon energies of 110 to 113 eV. This bump originates in weak Ce 4*f* multiplets, as was shown by early x-ray absorption spectroscopy studies on α- and γ-Ce metal [32].

Having identified the Ce 4*f* states, we next discuss the states between 5 to 8 eV BE (feature labeled C in figure 3(a)). These states correspond to the Ag 4*d* states in the valence band, as Ag 4*d* states have much higher cross-sections at these low photon energies compared to Sb 5*s* and 5*p* states. As seen in figure 4, the CIS spectrum for the spectral feature labeled C shows a small dip for photon energies between 110 to 113 eV, followed by a stronger reduction on increasing the incident photon energy from $h\nu = 114$ to 121 eV. On further increasing the photon energy above 121 eV, the states between 5 to 8 eV BE show a flattening between 121 to 125 eV, followed by a dip at higher photon energies. The overall behavior of the spectral intensity changes for states between 5 to 8 eV BE suggests an anti-resonance compared to the Ce 4*f* states coupled with the Cooper minimum of Ag 4*d* states [33]. As reported by Molodtsov *et al* [34] Ag metal exhibits at least two Cooper minima, which was analyzed to be arising from interference effects between $d \rightarrow f$ and $d \rightarrow p$ initial to final state dipole transition channels, and this results in a shift of the atomic (free atom) Ag Cooper minimum from 120 eV down to 60–80 eV and the creation of a secondary interference minimum at a higher energy of 150–160 eV. Thus, in $CeAgSb_2$, the Ag 4*d* states do not behave as in Ag metal, because the Ag atoms are further apart from each other in $CeAgSb_2$ than in Ag metal. Instead, they show a typical Cooper minimum energy dependence as

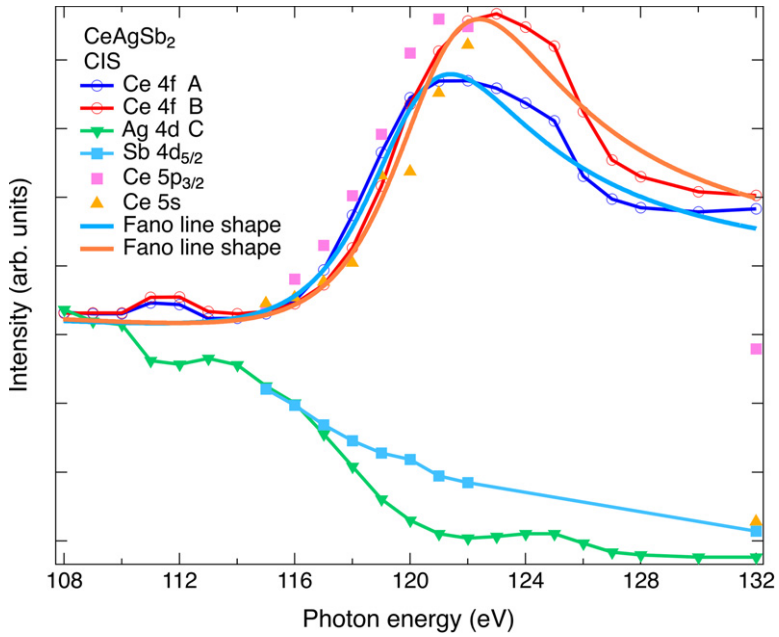

Figure 4. The constant initial state spectrum for Ce 4*f*, Ce 5*s*, Ag 4*d*, and Sb 4*d* states of $CeAgSb_2$ for photon energies from 108 to 132 eV. The Fano lineshape spectrum shown by solid lines overlaid on the CIS spectra for features A and B confirm the Ce 4*d*–4*f* resonance behavior.

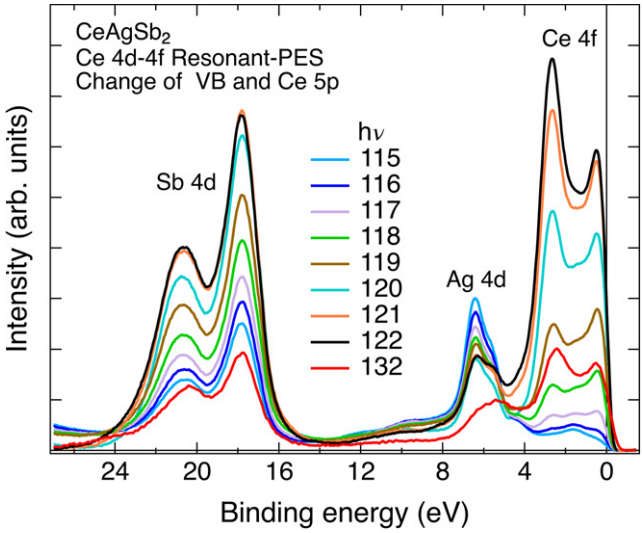

Figure 5. The photon energy dependent valence band along with the Ce 5*p* shallow core-level spectra measured at $T = 80$ K, showing the resonance enhancement of the Ce 5*p* core level spectra across the Ce 4*d*–4*f* resonance.

reported in atomic photoionization cross-section tables [33]. In addition, while we see a very weak intensity feature at about 10 eV BE in figure 3(a), it is more clearly seen in figure 5 which shows data measured up to much higher BEs including the Ce 5*p* shallow core-levels. Further, a weak but clear feature at about 1.7 eV BE labeled D is seen in figure 3(a) and also in figure 5 for incident photon energies of 115 to 118 eV. The 10 eV BE feature is due to the Sb 5*s* states and the 1.7 eV feature is due to Sb 5*p* states, as was observed in HAXPES of $CeAgSb_2$ [35].

In figure 5, we plot the photon energy dependent valence band along with the Ce 5*p* shallow core-level, which occurs between BEs of 16 to 24 eV. The spectral intensity of Ce 5*p* core-level show a systematic increase on increasing the photon energy from 115 to 122 eV. This matches with the resonant enhancement of Ce 4*f* valence states, as seen from the spectral intensity variation of Ce 5*p* states plotted along with the Ce 4*f* CIS spectra in figure 4. While we have not measured for higher photon energies beyond the maximum with small energy steps, the spectrum measured at a higher photon energy $h\nu = 132$ eV shows a clear reduction in spectral intensity.

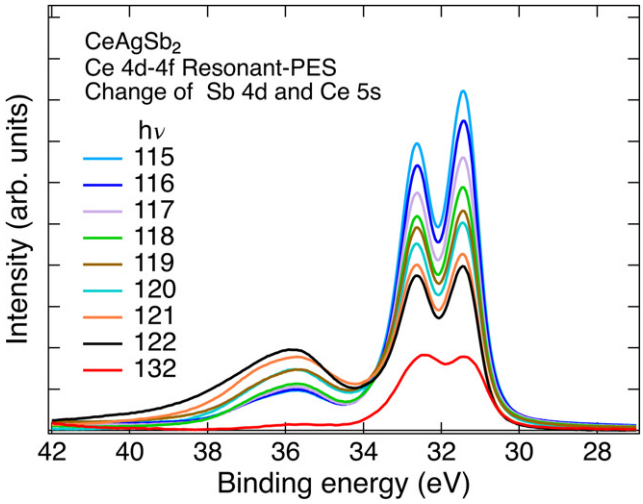

Figure 6. The Ce 5*s* and the Sb 4*d* core-level spectra measured as a function of photon energy for $h\nu = 115$ to 132 eV at $T = 80$ K.

Similarly, the Ce 5*s* and the Sb 4*d* core-level spectra were measured as a function of photon energy $h\nu = 115$ to 132 eV as shown in figure 6. The Ce 5*s* states at BE between 34 to 40 eV also show a clear intensity increase matching the changes seen in Ce 5*p* and 4*f* states. A similar enhancement of the Ce 5*s* and 5*p* shallow core-levels which matched the resonant enhancement of Ce 4*f* states was reported by Lenth *et al* [25] for Ce^{3+} pentaphosphates. The authors could demonstrate that the so called giant resonance maximum of the Ce 4*f*, 5*p* and 5*s* states across the 4*d* threshold can be understood by taking into account appropriate intermediate states associated with the Ce 5*s* and 5*p* states which lie at BEs between the Ce 4*d* and 4*f* states. Thus starting with the $4d^{10}4f^{1}5s^{2}5p^{6}$ initial state, the 4*d*–4*f* XAS process corresponds to $4d^{9}4f^{2}5s^{2}5p^{6}$ excitation. The resonances in Ce 4*f*, 5*p* and 5*s* then corresponds to the usual autoionization of the excited state $4d^{9}4f^{2}5s^{2}5p^{6}$ via the states $4d^{10}4f^{0}5s^{2}5p^{6}$ + e, $4d^{10}4f^{1}5s^{2}5p^{5}$ + e and $4d^{10}4f^{1}5s^{1}5p^{6}$ + e configurations, respectively. The present results of resonances in the Ce 5*p* and 5*s* shallow core levels of $CeAgSb_2$ are similarly attributed to autoionization of the excited $4d^{9}4f^{2}$ via intermediate $5s^{1}5p^{6}$ and $5s^{2}5p^{5}$ states.

Interestingly, the Sb 4*d* core-level spectra as a function of photon energy shows opposite behavior to the Ce derived states, that is, they show a systematic reduction in spectral intensity when the Ce states show a systematic increase in spectral intensities. However, the reduction in the spectral intensity of Sb derived anionic shallow core-level states also follows the decrease expected from atomic photoionization cross-sections [33].

In figure 7, we show the photon energy dependence ($h\nu = 115$ to 122 eV) of weak spectral features over the BE range from 43 to 65 eV, which correspond to the Ce NNV Auger features. The Ce NNV features overlap the Ag 4*p* states which occur at 58.13 and 60.73 eV BE, and the plasmon feature of Sb 4*d* states at about 47 eV BE. The plasmon feature occurs at ∼15.7 eV higher BE from Sb 4*d* core levels, as observed using core-level HAXPES [35]. The wider BE range spectrum showing the Sb 4*d* and Ce 5*s* states are shown in the inset for incident photon energies of 115 and 122 eV. The systematic shift of the broad feature (double-headed arrow in figure 7) is attributed to the shift of the Ce NNV Auger features, which track the change in the incident photon energy. This was confirmed by carrying out fits to the spectra obtained with $h\nu = 119$ to 121 eV as shown in figure 8. The fitted spectra show that the Ce NNV states shift systematically (dashed lines in figure 8), while the Ag 4*p* features occur at 58.13 and 60.73 eV, and a broad Sb 4*d* plasmon feature occurs at about 47.1 eV BE. For lower ($h\nu = 115$ to 118 eV) and higher ($h\nu = 122$ eV) photon energies, it was not possible to obtain reliable fits, because the Auger spectra overlapped the Sb 4*d* plasmon or the Ag 4*p* states. Thus, we could account for all the spectral changes occurring in Ce, Ag and Sb derived states for photon energies scanned across the Ce 4*d*–4*f* threshold.

We then carried out XAS across the Ce 3*d*–4*f* $M_{4,5}$-edges at $T = 25$ K and 300 K as shown in figure 9. The spectra consist of the spin–orbit split M_5 and M_4-edges with main peaks positioned at photon energies $h\nu = 881$ eV and 898.2 eV, respectively. The spectra also show weak hump structures (asterisk marks in figure 9) positioned at about 887 eV and 904 eV at photon energies above the M_5 and M_4 main peaks, respectively. It is well-known that the main peaks of the M_5 and M_4 edges correspond to the $f^1 \rightarrow f^2$ excitations while the weak hump feature is associated with the $f^0 \rightarrow f^1$ excitation, indicative of Kondo screening in the XAS spectra. The spectra are normalized at the M_4-edge peak as the temperature dependent changes are larger in the $f^0 \rightarrow f^1$ excitation of the M_4-edge. This makes it easier to compare the temperature dependent changes in the $f^0 \rightarrow f^1$ excitation with the calculated spectra also shown in figure 9.

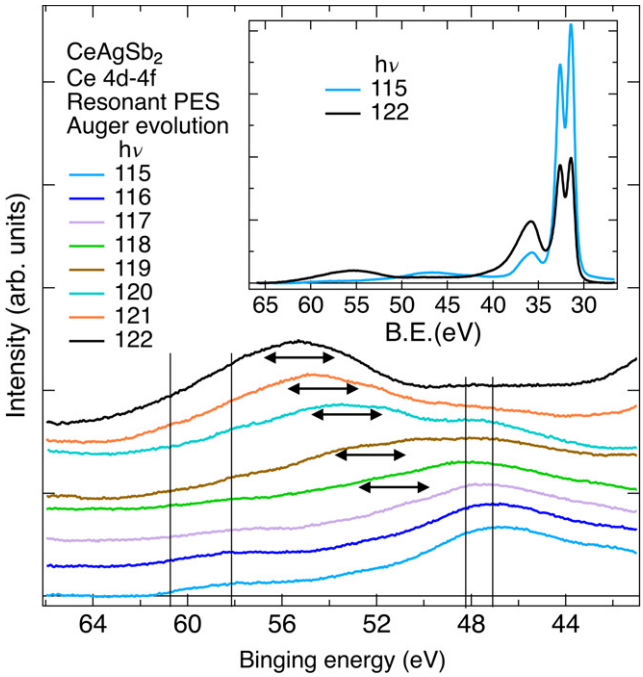

Figure 7. The photon energy dependence ($h\nu = 115$ to 122 eV) of weak spectral features over the BE range from 43 to 65 eV, which correspond to the Ce NNV Auger features (double headed arrows). They overlap the Ag 4*p* states (vertical lines at 58.2 and 60. 6 eV BE) and the expected plasmon features (vertical lines at ∼47.0 and ∼48.3 eV) of Sb 4*d* states.

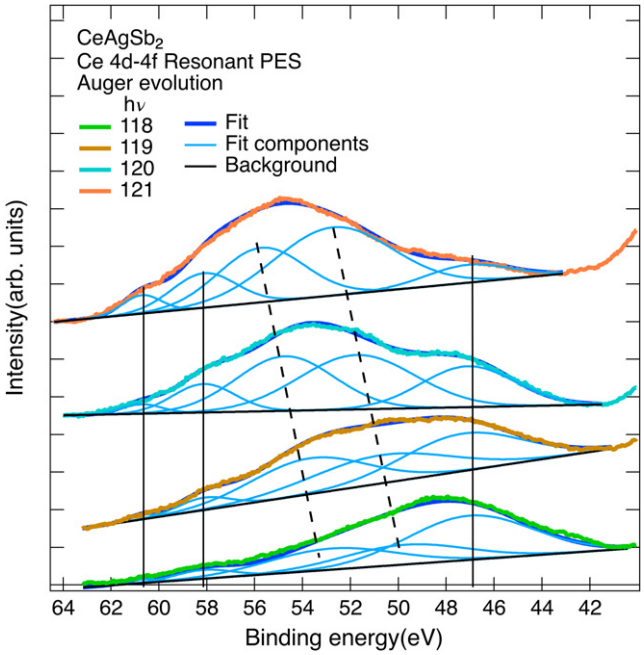

Figure 8. The fits to the Ce NNV Auger features (dashed lines), including the overlapping the Ag 4*p* states (vertical lines at 58.2 and 60 6 eV BE) and a single broad peak approximating the plasmon excitations (vertical line at ∼47 eV BE) of Sb 4*d* states.

The $M_{4,5}$ absorption spectra of intermediate valent Ce compounds can be simulated in the framework of the SIAM [38], but this approach neglects the multiplet effects. As these effects determine the shape of the $M_{4,5}$ absorption spectra, we have calculated the XAS spectra using a full multiplet configuration interaction code (Quanty [36, 37]). Such an approach can be considered as a full multiplet calculation combined with a simplified SIAM approach where the band states are represented by a single ligand state. The hybridization between 4*f* states leads to a ground state which is a mixture of the different configurations $|\Psi_{GS}\rangle = C_0|f^0\rangle + C_1|f^1\underline{L}\rangle + C_2|f^2\underline{L}^2\rangle$ where $\underline{L}$ denotes a ligand hole. Moreover, we introduce the experimentally known crystal-field spectrum with a Γ_6 ground state corresponding to $J_z = |\pm\frac{1}{2}\rangle$ separated from two

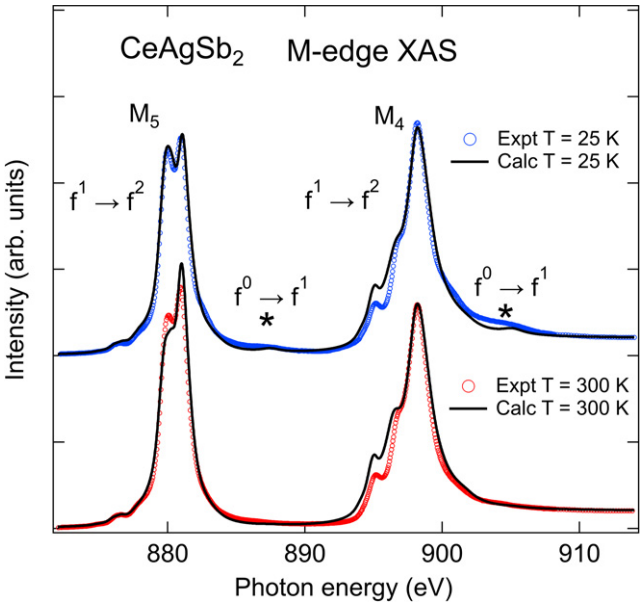

Figure 9. The M-edge XAS of $CeAgSb_2$ measured at $T = 25$ K and 300 K compared with simplified SIAM calculations at $T = 25$ K and 300 K. The main M_5 and M_4 peaks correspond to the $f^1 \rightarrow f^2$ excitations while the asterisks mark the weak feature associated with the $f^0 \rightarrow f^1$ excitation. The spectra are normalized at the M_4-edge peak as the temperature dependent changes are larger in the $f^0 \rightarrow f^1$ excitation.

excited Γ_7 excited states corresponding to $J_z = |\pm\frac{3}{2}\rangle$ and $J_z = |\pm\frac{5}{2}\rangle$ by ∼5 meV and ∼12 meV, respectively [10, 14]. The hybridization between 4*f* and ligand state lead to the formation of a singlet ground state and a triplet excited state both originating from the Γ_6 crystal field level. Such a full multiplet configuration interaction does not give a realistic value for the Kondo energy (difference between the singlet and triplet states) [39]. Therefore to simulate the finite temperature spectra, we introduce the experimental Kondo temperature estimated to be $T_K = 65$ K from magnetic measurements [10, 13]. The finite temperature spectra ($T = 25$ K and 300 K) are then simulated from the spectra associated with the different initial states, the singlet, triplet and excited crystal field states weighted by the Boltzmann factor. As shown in figure 9, the best match with experimental spectra were obtained for the following electronic parameters: the 4*f* energy $\varepsilon_f = E(f^1\underline{L}) - E(f^0) = -2.4$ eV, the average Coulomb energy $U_{ff} = 8.5$ eV, the 3*d*–4*f* Coulomb interaction $U_{fc} = 12.45$ eV, the multipolar Slater parameters are atomic parameters scaled by factor of 0.8, and the hybridization between the 4*f* level and the ligand state, $V = 0.2$ eV. The calculation indicates a small finite mixed valency with an *f*-electron count of $n_f = 0.97$. While the $f^0 \rightarrow f^1$ spectral feature for the $T = 25$ K spectrum is reproduced fairly well in the calculations, the $T = 300$ K spectrum essentially looks like a pure trivalent Ce^{3+} configuration with negligible spectral weight in the $f^0 \rightarrow f^1$ spectral feature. The modification of the shape of the M_4 edge with temperature is due to the thermal population of the crystal field Γ_7 excited levels.

Finally, we have tried to address the role of Kondo screening in the Ce 4*f* states in the valence band spectra, which leads to the so-called f^1 feature near E_F associated with the tail of the Kondo resonance occurring above E_F. As can be seen in figure 3(a), the spectrum obtained with photon energy $h\nu = 119$ eV showed the maximum increase of feature A compared to feature B. We have first obtained the *f*-electron density of states as the difference spectrum of this resonantly enhanced spectrum by subtracting the off-resonance spectrum obtained with photon energy of $h\nu = 108$ eV (figure 10). In order to see changes very near and just above E_F, the difference spectrum was divided by the Fermi–Dirac (FD) function convoluted with the Gaussian function corresponding to the experimental resolution, following earlier work [40–42]. The obtained spectrum shows a weak structure at ∼0.3 eV BE and a small peak feature just above E_F, as seen in figure 10. Similarly, we also analyzed the *f*-electron contribution for the spectrum obtained with photon energy $h\nu = 123$ eV, and there too, we observe a weak structure at ∼0.3 eV BE and a small peak feature just above E_F as shown in figure 11. The ∼0.3 eV feature is due to the Ce $4f^1_{7/2}$ states while the feature just above E_F is due to the $4f^1_{5/2}$ character tail of the Kondo resonance above E_F. This indicates that states at E_F are renormalized by Kondo screening, leading to the moderate enhancement of the carriers in $CeAgSb_2$. It is noted that the nearly comparable intensity of the f^0 feature to the f^1 feature is attributed to the surface enhanced contribution to the f^0 feature at incident photon energies across the Ce 4*d*–4*f* threshold. This is consistent with known results on other Ce-based systems with low T_K, such as γ-Ce ($T_K \sim 100$ K) and CeAl ($T_K \sim 20$ K) [21], as well as CeB_6 ($T_K \sim 10$ K) [43].

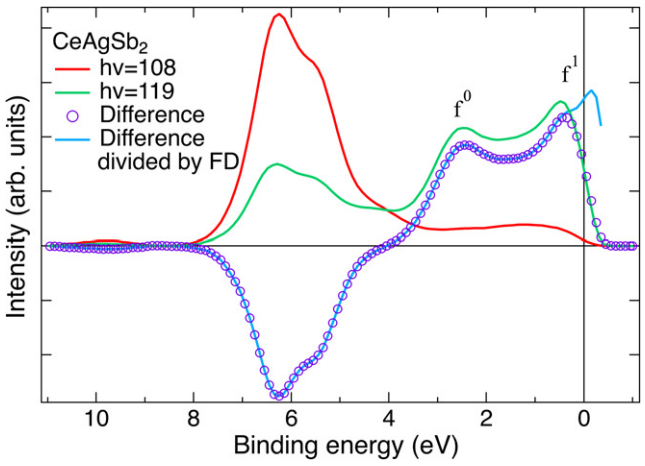

Figure 10. The difference spectrum divided by the FD function convoluted with the experimental Gaussian function showing the Kondo resonance f^1 feature near the Fermi level associated with the tail of the Kondo resonance occurring above the Fermi level. The spectrum obtained with photon energy $h\nu = 119$ eV shows the maximum increase of feature f^1 compared to feature f^0.

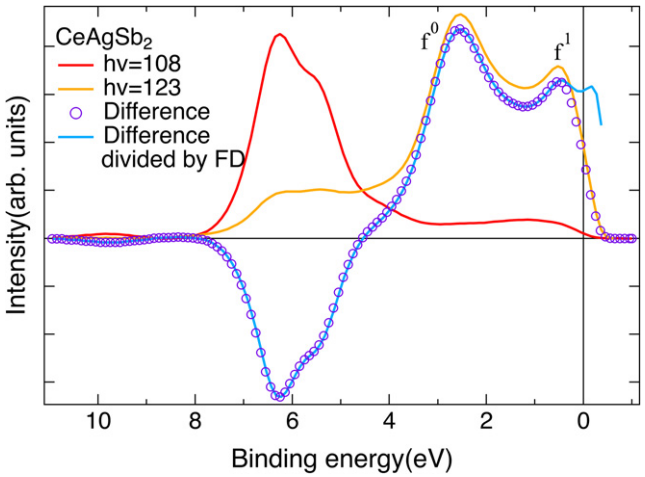

Figure 11. The difference spectrum divided by the FD function convoluted with the experimental Gaussian function showing the Kondo resonance f^1 feature near the Fermi level, associated with the tail of the Kondo resonance occurring above the Fermi level. The spectrum obtained with photon energy $h\nu = 123$ eV shows a weaker increase of feature f^1 compared to feature f^0.

These systems show a qualitatively similar 4*d*–4*f* on-resonance behavior with comparable intensities for the f^0 and f^1 features and a value of n_f in the range of 0.97–0.99, consistent with our analysis of $CeAgSb_2$.

4. Conclusions

In conclusion, we have investigated the electronic structure of $CeAgSb_2$ using Ce 4*d*–4*f* resonant photoemission spectroscopy of the valence band states of $CeAgSb_2$. The constant initial state spectra show different maxima for bulk and surface dominated Ce $4f^0$ and $4f^1$ states. The measured Ce 3*d*–4*f* *M*-edge XAS spectrum could be simulated with a simplified SIAM calculation with full atomic multiplets, and the bulk Ce 4*f* electron count could be determined in $CeAgSb_2$. We also investigated the resonant photoemission behavior of Ce 5*s* and 5*p* core-levels, and the simultaneous suppression of Sb 4*d* core-level and Ag 4*d* valence band states across the Ce 4*d*–4*f* threshold. The Ce 5*s* states show an exchange splitting which confirm the local magnetic moment of Ce 4*f* states. The results characterize the Ce 4*f* states and indicate the role of Kondo screening in forming the moderately enhanced heavy-fermion carriers in $CeAgSb_2$.

Acknowledgments

DM, CMC and AC thank the France-Taiwan (CNRS-MOST) bilateral project for financially supporting this research under Contract No. CNRS 290771 and Contract No. MOST 109-2911-I-213-501. AC thanks the Ministry of Science and Technology of the Republic of China, Taiwan, for financially supporting this research under Contract No. MOST 108-2112-M-213-001-MY3.

Data availability statement

All data that support the findings of this study are included within the article (and any supplementary files).

ORCID iDs

C-M Cheng https://orcid.org/0000-0002-7569-6757
C-S Lue https://orcid.org/0000-0002-3074-9253
A Chainani https://orcid.org/0000-0002-5639-5393

References

[1] Doniach S 1977 The phase diagram of the Kondo lattice *Valence Instabilities and Related Narrow-Band Phenomena* ed R D Parks (New York: Plenum) p 169
[2] Fulde P 1991 *Electron Correlations in Molecules and Solids* (*Springer Series on Solid State Sciences* vol 100) (Berlin: Springer)
[3] Hewson A C 1993 *The Kondo Problem to Heavy Fermions* (Cambridge: Cambridge University Press)
[4] Malterre D, Grioni M and Baer Y 1996 *Adv. Phys.* **45** 299
[5] Allen J W 2005 *J. Phys. Soc. Japan* **74** 34
[6] Sengupta K *et al* 2004 *Phys. Rev.* B **70** 064406
[7] Nakano T, Onuma S, Takeda N, Uhlov K, Jan P, Sechovsk V, Gouchi J and Uwatoko Y 2019 Coexistence of localized and heavy itinerant states in antiferromagnetic $CePtGe_2$ *Phys. Rev.* B **100** 035107
[8] Sologub O, Noël H, Leithe-Jasper A, Rogl P and Bodak O I 1995 *J. Solid State Chem.* **115** 441
[9] Chainani A *et al* 2014 Electronic structure of $CeCuAs_2$ *Phys. Rev.* B **89** 235117
[10] Araki S, Metoki N, Galatanu A, Yamamoto E, Thamizhavel A and Onuki Y 2003 Crystal structure, magnetic ordering, and magnetic excitation in the 4*f* -localized ferromagnet $CeAgSb_2$ *Phys. Rev.* B **68** 024408
[11] Takeuchi T *et al* 2003 *Phys. Rev.* B **67** 064403
[12] Nakashima M *et al* 2003 *J. Phys.: Condens. Matter* **15** L111
[13] Jobiliong E, Brooks J S, Choi E S, Lee H and Fisk Z 2005 Magnetization and electrical-transport investigation of the dense Kondo system $CeAgSb_2$ *Phys. Rev.* B **72** 104428
[14] Dann J A, Hillier A D, Armitage J G M and Cywinski R 2000 *Physica* B **38** 289290
[15] Sidorov V A, Bauer E D, Frederick N A, Jeffries J R, Nakatsuji S, Moreno N O, Thompson J D, Maple M B and Fisk Z 2003 *Phys. Rev.* B **67** 224419
[16] Gunnarsson O and Schönhammer K 1983 *Phys. Rev. Lett.* **50** 604
Gunnarsson O and Schönhammer K 1983 *Phys. Rev.* B **28** 4315
[17] Fuggle J C, Hillebrecht F U, Esteva J-M, Karnatak R C, Gunnarsson O and Schönhammer K 1983 *Phys. Rev.* B **27** 4637
[18] Arakane T, Sato T, Souma S, Takahashi T, Watanabe Y and Inada Y 2007 *J. Magn. Magn. Mater.* **310** 396
[19] Saitoh Y *et al* 2016 Electronic structures of ferromagnetic $CeAgSb_2$: soft x-ray absorption, magnetic circular dichroism, and angle-resolved photoemission spectroscopies *J. Phys. Soc. Japan* **85** 114713
[20] Fujiwara H *et al* 2020 Strongly correlated electron systems (SCES2019) *JPS Conf. Proc.* vol 30 p 011101
[21] Duò L, Rossi S D, Vavassori P, Ciccacci F, Olcese G L, Chiaia G and Lindau I 1996 *Phys. Rev.* B **54** R17363
[22] Chiaia G *et al* 1998 *Phys. Rev.* B **57** 12030
[23] Cohen R L, Wertheim G K, Rosencwaig A and Guggenheim H J 1972 Multiplet splitting of the 4*s* and 5*s* electrons of the rare earths *Phys. Rev.* B **5** 1037
[24] Rao C N R and Sarma D D 1980 *Chemistry and Technology of Rare Earths* (New York: Academic)
[25] Lenth W, Lutz F, Barth J, Kalkoffen G and Kunz C 1978 *Phys. Rev. Lett.* **41** 1185
[26] Allen J W, Maple M B, Kang J-S, Yang K N, Torikachvili M S, Lassailly Y, Ellis W P, Pate B B and Lindau I 1990 *Phys. Rev.* B **41** 9013
[27] Kakizaki A, Harasawa A, Ishii T, Kashiwakura T, Kamata A and Kunii S 1995 *J. Phys. Soc. Japan* **64** 302
[28] Iwasaki T *et al* 2002 *Phys. Rev.* B **65** 195109
[29] Sekiyama A, Iwasaki T, Matsuda K, Saitoh Y, Ônuki Y and Suga S 2000 *Nature* **403** 396
[30] Cho E-J *et al* 2003 *Phys. Rev.* B **67** 155107
[31] Banik S, Chakrabarti A, Joshi D A, Thamizhavel A, Phase D M, Dhar S K and Deb S K 2010 *Phys. Rev.* B **82** 113107
[32] Haensel R, Rabe P and Sonntag B 1970 *Solid State Commun.* **8** 1845
[33] Yeh J J and Lindau I 1985 *At. Data Nucl. Data Tables* **32** 1–155
[34] Molodtsov S L, Halilov S V, Servedio V D P, Schneider W, Danzenbächer S, Hinarejos J J, Richter M and Laubschat C 2000 Cooper minima in the photoemission spectra of solids *Phys. Rev. Lett.* **85** 4184
[35] Chainani A *et al* unpublished
[36] Haverkort M W, Zwierzycki M and Andersen O K 2012 *Phys. Rev.* B **85** 165113
[37] Haverkort M W 2016 *J. Phys.: Conf. Ser.* **712** 012001
[38] Gunnarsson O and Schönhammer K 1983 *Phys. Rev.* B **28** 4315

[39] Strigari F *et al* 2015 Quantitative study of valence and configuration interaction parameters of the Kondo semiconductors CeM_2Al_{10} (M = Ru, Os and Fe) by means of bulk-sensitive hard x-ray photoelectron spectroscopy *J. Electron Spectrosc. Relat. Phenom.* **199** 56
[40] Greber T, Kreutz T J and Osterwalder J 1997 *Phys. Rev. Lett.* **79** 4465
[41] Reinert F, Ehm D, Schmidt S, Nicolay G, Hüfner S, Kroha J, Trovarelli O and Geibel C 2001 *Phys. Rev. Lett.* **87** 106401
Ehm D, Hufner S, Reinert F, Kroha J, Wolfle P, Stockert O, Geibel C and Lohneysen H v 2007 *Phys. Rev.* B **76** 045117
[42] Matsunami M *et al* 2009 *Phys. Rev. Lett.* **102** 036403
[43] Chiaia G *et al* 1997 *Phys. Rev.* B **55** 9207